nature communications

Article

https://doi.org/10.1038/s41467-025-58051-7

Realization of a three-dimensional photonic higher-order topological insulator

Received: 16 April 2024

Accepted: 11 March 2025

Ziyao Wang[1,8], Yan Meng[2,8], Bei Yan[3,8], Dong Zhao[1,8], Linyun Yang[4], Jingming Chen[1], Minqi Cheng[1], Tao Xiao[1], Perry Ping Shum[1], Gui-Geng Liu[5], Yihao Yang[6], Hongsheng Chen[6], Xiang Xi[2] ✉, Zhen-Xiao Zhu[1] ✉, Biye Xie[7] ✉ & Zhen Gao[1] ✉

The discovery of photonic higher-order topological insulators (HOTIs) has expanded our understanding of band topology, offering robust lower-dimensional boundary states for photonic devices. However, realizing three-dimensional (3D) photonic HOTIs remains challenging due to the vectorial and leaky nature of electromagnetic waves. Here, we present the experimental realization of a 3D Wannier-type photonic HOTI using a tight-binding-like metal-cage photonic crystal, whose band structures align with a 3D tight-binding model via confined Mie resonances. Microwave near-field measurements reveal coexisting topological surface, hinge, and corner states in a single 3D photonic HOTI, consistent with theoretical predictions. Remarkably, these states are robust and self-guided even within the light cone continuum, functioning without ancillary cladding. This work paves the way for multi-dimensional manipulation of electromagnetic waves on 3D cladding-free photonic bandgap materials, enabling practical applications in 3D topological integrated photonic devices.

Recently, the discovery of higher-order band topology[1–3] has revolutionized the study of topological matters with unconventional bulk-boundary correspondence that enables lower-dimensional topological boundary states in at least two dimensions lower than the bulk, in contrast to the conventional first-order topological matters whose topological boundary states only live in just one dimension lower than the bulk. For example, the first-order (higher-order) topological phases host topological edge (corner) states in a two-dimensional (2D) system and topological surface (hinge or corner) states in a three-dimensional (3D) system. To date, extensive studies of various higher-order topological phases have been carried out in condensed matter physics[4,5], photonics[6–26], acoustics[27–42], mechanics[43,44], electric circuits[45,46], and even thermal diffusions[47,48].

Generally, from the dimensional perspective, higher-order topological phases can be classified into two major classes: 2D[6–19,27–30,43–45,47,48] and 3D[20–25,31–42,46,49]. Compared with the 2D higher-order topological phases whose topological boundary states are limited to first-order one-dimensional (1D) edge states and second-order zero-dimensional (0D)

---

[1]State Key Laboratory of Optical Fiber and Cable Manufacture Technology, Department of Electronic and Electrical Engineering, Guangdong Key Laboratory of Integrated Optoelectronics Intellisense, Southern University of Science and Technology, Shenzhen 518055, China. [2]School of Electrical Engineering and Intelligentization, Dongguan University of Technology, Dongguan 523808, China. [3]Hubei Province Key Laboratory of Systems Science in Metallurgical Process, and College of Science, Wuhan University of Science and Technology, Wuhan 430081, China. [4]College of Aerospace Engineering, Chongqing University, Chongqing 400030, China. [5]Research Center for Industries of the Future, Department of Electronic and Information Engineering, School of Engineering, Westlake University, Hangzhou 310030, China. [6]Interdisciplinary Center for Quantum Information, State Key Laboratory of Modern Optical Instrumentation, ZJU-Hangzhou Global Science and Technology Innovation Center, College of Information Science and Electronic Engineering, ZJU-UIUC Institute, Zhejiang University, Hangzhou 310027, China. [7]School of Science and Engineering, The Chinese University of Hong Kong, Shenzhen 518172, China. [8]These authors contributed equally: Ziyao Wang, Yan Meng, Bei Yan, Dong Zhao. ✉e-mail: xix@dgut.edu.cn; zhuzx@sustech.edu.cn; xiebiye@cuhk.edu.cn; gaoz@sustech.edu.cn

corner states, 3D higher-order topological phases can host first-order 2D surface states, second-order 1D hinge states, and third-order 0D corner states, significantly benefiting multi-dimensional wave manipulation and increasing device integration density. More specifically, there are two different types of 3D HOTIs: 3D HOTIs derived from the generalized Su-Schrieffer-Heeger (SSH) model without quantized multipole moments which are termed Wannier-type 3D HOTIs[31–33], and 3D HOTIs with quantized multipole moments which are dubbed as octupole HOTIs[34,35]. Compared with the octupole HOTIs, the Wannier-type 3D HOTIs don't require negative nearest-neighbor couplings and have been experimentally realized in acoustic crystals[31–33] and electric circuits[46] by directly mimicking a 3D SSH model. However, due to the vectorial nature of electromagnetic waves and the lack of mirror reflection symmetry in the vertical direction, the eigenmodes in 3D photonic crystals cannot be simplified as scalar transverse electric (TE) or transverse magnetic (TM) modes. This results in complex band dispersions, making it challenging to describe 3D photonic systems using a simple tight-binding model[50,51]. Consequently, in contrast to the extensive experimental realizations of 3D HOTIs in acoustics and electric circuits, their photonic counterparts have been severely lagged, with only a handful of experimental demonstrations of higher-order Dirac[20] or Weyl[21] semimetals with topological hinge states in 3D photonic crystals. However, due to the absence of complete 3D photonic bandgaps in photonic higher-order Dirac or Weyl semimetals, the topological hinge states only exist in a limited range of k_z and could be scattered into the bulk when encountering obstacles, which inevitably jeopardizes their efficient and robust transport. A natural question arises as to whether there exist 3D photonic HOTIs with complete 3D photonic bandgaps and hosting first-order topological surface states, second-order topological hinge states, and third-order topological corner states in the whole Brillouin zone (BZ). More recently, several 3D photonic HOTIs have been theoretically proposed in tight-binding-like photonic crystals based on the confined Mie resonance[22–24]. However, to date, 3D photonic HOTIs have never been experimentally realized in any photonic system.

Here, we report on the experimental realization of a Wannier-type 3D photonic HOTI in a tight-binding-like photonic crystal, which can be regarded as a photonic realization of the celebrated 3D SSH model. The tight-binding-like photonic crystals comprise coupled dielectric rods embedded with metallic pillars, forming confined Mie resonances and supporting exponentially decayed modes. These exponentially decayed modes function as artificial atomic orbitals, resembling tight-binding models with nearest-neighbor couplings and exhibiting nearly identical band structures. By direct microwave real-space visualization and momentum-space spectroscopy measurements, we experimentally observe coexisting self-guided topological surface states on 2D surfaces, topological hinge states on 1D hinges, and topological corner states confined to 0D corners in a single 3D tight-binding-like photonic crystal without extra claddings, manifesting a dimensional hierarchy of topological boundary states due to the third-order band topology. Furthermore, we experimentally demonstrate that the topological surface, hinge, and corner states are robust against defects. Our work provides a versatile platform to design 3D topological photonic crystals by directly mimicking the tight-binding models, which may inspire the future design of 3D topological integrated photonic devices and chips.

Results

Design of a Wannier-type 3D photonic HOTIs

We begin with a 3D SSH model whose unit cell contains eight sites (blue spheres) coupled with nearest-neighbor intercell (t_v and t_{zv}) and intracell (t_w and t_{zw}) couplings, as shown in Fig. 1a. When the intercell couplings t_v (t_{zv}) are larger than the intracell couplings t_w (t_{zw}), the 3D SSH model exhibits a Wannier-type third-order topological insulating phase with complete 3D bandgaps and coexisting topological surface,

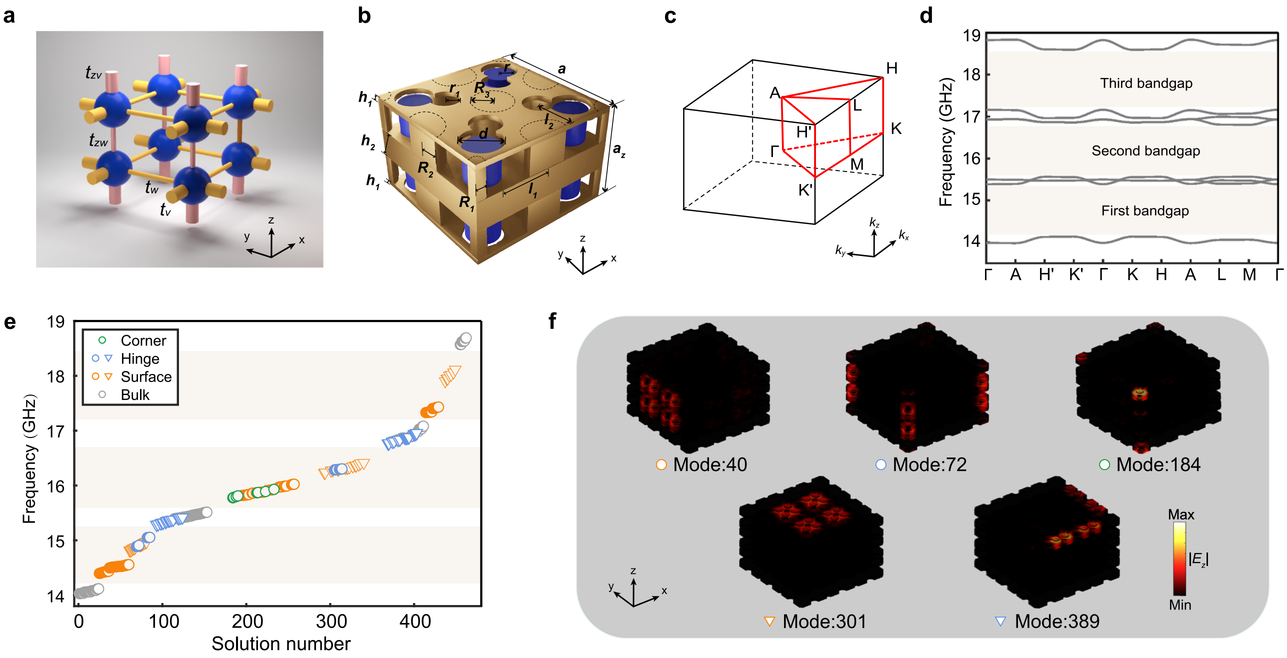

Fig. 1 | Design of a 3D photonic HOTI. a Schematic of the 3D SSH model, the blue spheres represent the eight sites, and the pink (yellow) rods represent the vertical (planar) intracell and intercell nearest-neighbor couplings. **b** Unit cell of the 3D MCPC. The golden parts represent the perforated metallic parallel plates and metallic pillars, and the blue parts represent the dielectric rods. The lattice constants in the x-y plane and z-direction are $a = 15$ mm and $a_z = 10$ mm, respectively. The other geometrical parameters are $R_1 = 1$ mm, $R_2 = R_3 = 2$ mm, $h_1 = 0.5$ mm, $h_2 = 3$ mm, $r = 1.6$ mm, $r_1 = 1.5$ mm, $d = 1.9$ mm, $l_1 = 5$ mm, $l_2 = 4.5$ mm, respectively. **c** 3D BZ of the MCPC. **d** Simulated bulk band structure of the 3D MCPC along high-symmetry lines, the floral white regions represent the three photonic bandgaps. **e** Simulated eigenstate spectrum of a finite 3D MCPC with 3 × 3 × 3 unit cells. The bulk, surface, hinge, and corner states are represented by grey, orange, blue, and green triangles and circles, respectively. For the surface and hinge states, circles (triangles) indicate these states located at the x-z or y-z plane (x-y plane). **f** Simulated field distributions of the eigenmodes corresponding to the surface, hinge, and corner states labeled in **e**, respectively.

hinge, and corner states (see Note 1 in Supplementary Materials)[31–34]. Moreover, the nontrivial higher-order band topology of the 3D SSH model can be characterized by quantized Wannier centers (see Note 2 in Supplementary Materials) and the dimensional hierarchy of the topological states (see Note 3 in Supplementary Materials). To implement the 3D SSH model in a photonic system, we adopt a 3D tight-binding-like metal-cage photonic crystal (MCPC)[22] whose unit cell is shown in Fig. 1b, where eight dielectric rods (blue color) are placed between three parallel perforated metallic plates (golden color) serving as the eight sites and each dielectric rod is surrounded by four metallic pillars (golden color) to confine the slowly decaying Mie resonances' states, leading to the vectorial electromagnetic waves in 3D photonic crystals being simplified to the scalar-wave-like ones (only TM-like modes) and the 3D MCPC exhibits almost the same scalar-wave-like band structures as those of the 3D tight-binding models (see Notes 4 in Supplementary Materials). In the context of MCPC, the planar (vertical) intracell and intercell couplings can be modulated by the radii R_1 and R_2 of the metallic rods and the distance R between the dielectric rods and the central metallic rods (the radius r_1 of the air holes and the thickness h_1 and h_2 of the metallic plates). Since all nearest-neighbor couplings can be modulated independently and flexibly by tuning the geometrical parameters of the MCPCs, a third-order 3D MCPC can be obtained by setting $R_1 = 1$ mm, $R_2 = R_3 = 2$ mm, $h_1 = 0.5$ mm, $h_2 = 3$ mm, $r = 1.6$ mm, $r_1 = 1.5$ mm, $d = 1.9$ mm, $l_1 = 5$ mm, $l_2 = 4.5$ mm, $a = 15$ mm, $a_z = 10$ mm, respectively. The simulated bulk band structure of the third-order 3D MCPC in the first BZ (Fig. 1c) is shown in Fig. 1d, which has three complete photonic bandgaps (floral white regions) and bears a close resemblance to that of the 3D SSH model (see Note 5 in Supplementary Materials). To further unveil the third-order band topology of the 3D MCPC, we design a finite 3D MCPC with $3 \times 3 \times 3$ unit cells and calculate its eigenstates spectrum, as shown in Fig. 1e, we use symbols of different colors and shapes to distinguish topological states and their eigenmode distributions. Although the topological surface, hinge, and corner states exhibit a downward frequency shift compared to those of the tight-binding model due to a slight chiral symmetry breaking of the bulk band of the MCPC (see Note 5 in Supplementary Materials), these topological states still coexist in a single 3D MCPC with a third-order band topology. The simulated E_z field distributions of the topological surface, hinge, and corner eigenstates are shown in Fig. 1f. It can be seen that for the topological surface, hinge, and corner states, their E_z fields are mainly localized at the 2D surfaces, 1D hinges, and 0D corners of the 3D MCPC, respectively, matching well with the tight-binding results.

Experimental observation of the first-order photonic topological surface states

Now we start experimentally demonstrating the first-order topological surface states in the 3D MCPC. The fabricated experimental sample is shown in Fig. 2a, which consists of 20 unit cells along the x and z directions and 4 unit cells in the y direction. To show the detailed configuration of each layer, the compositional layers are glided for clarity, as shown in Fig. 2b, where the perforated copper plates (golden color) with air holes are adopted to induce vertical interlayer and intralayer couplings, and the perforated air foams (white color) are used to fix the metallic and dielectric rods. Note that all six surfaces of the 3D MCPC can support topological surface states and here we only focus on the front (010) surface (parallel to the x-z plane). Figure 2d presents the calculated topological surface state dispersions (orange lines) along high-symmetry lines of the projected 2D surface BZ (Fig. 2c) and the light cone is indicated by the cyan curve. It can be seen that the first-order topological surface states exist within all three photonic bandgaps and are completely separated from the bulk bands (grey lines). More interestingly, the topological surface states exhibit a well-defined dispersion even within the light cone continuum, indicating the leakage of topological surface states to the surrounding air is omittable in the whole surface BZ. This counterintuitive phenomenon stems from the strong field localization of confined Mie resonances, which concentrate the electric fields around the dielectric rods of the 3D MCPCs with minimal surface leakage. Meanwhile, the wave functions of the topological surface states decay evanescently and retain the vectorial nature of surface electromagnetic waves. This unique property gives rise to the field texture of topological surface states resembling a Néel-type skyrmion[52] (see Note 6 in Supplementary Materials). This characteristic allows us to observe stable topological surface states across the entire surface BZ, even within the light cone continuum. This is nontrivial since conventional photonic topological surface states either need ancillary cladding to prevent the leakage[53–55] or generally have a large radiative loss inside the light cone making them unobservable[56]. We also calculate topological surface states' quality factor (Q factors) in the third bandgap (see Note 6 in Supplementary Materials). The high Q factors indicate that the photonic topological surface states of the MCPCs are self-guided without extra cladding and well-localized even in the light cone continuum. Moreover, with additional surface modifications, the Q factor of topological surface states can be further increased (See Note 7 in Supplementary Materials). We then perform experiments to measure the transmission spectra of the topological surface (orange color) and bulk (dark grey) states by placing a source antenna (cyan stars in Fig. 2f–g) at the center of the front (010) surface and inserting a probe antenna into the surface or bulk, respectively, as shown in Fig. 2e. Three photonic bandgaps (floral white color) can be observed as the bulk transmission spectrum exhibits three broad dips in the frequency ranges of 14.2–15.2, 15.3–16.8, and 17–18 GHz, respectively. Within the photonic bandgaps, the surface state transmission spectrum exhibits three sharp peaks, indicating the existence of topological surface states on the 3D MCPC surfaces. To directly observe the field distributions of the topological surface states, we employ a probe antenna to measure the electric field distributions of the topological surface states across the entire structure (see Methods). The measured electric field distribution of the topological surface state at 14.6 GHz is shown in Fig. 2f, which agrees well with the simulation results shown in Fig. 2g. The field is predominantly localized on the sample's surface, signifying the existence of topological surface states. By Fourier-transforming the measured complex electric field distributions from real space to reciprocal space, we obtain the measured surface state dispersion along the high-symmetry lines $\bar{\Gamma} - \bar{A} - \bar{H} - \bar{K} - \bar{\Gamma}$ in the projected 2D BZ, as shown in Fig. 2h, the measured results (color map) demonstrate excellent consistency with the simulated surface state dispersion (white dashed line).

Experimental observation of the second-order photonic topological hinge states

Next, we experimentally demonstrate the second-order photonic topological hinge states originating from the higher-order band topology of the 3D MCPC. Note that all twelve hinges support topological hinge states. Here we only focus on one hinge between (100) and (010) surfaces and simulate its eigenmode dispersion relationship along the k_z direction, as shown in Fig. 3a, the surface states, hinge states, bulk states, and light cone are indicated by the orange, blue, grey and cyan lines, respectively. Similar to the topological surface states, the simulated eigenmode field distribution of the hinge state (Fig. 3b) marked by a black triangle in Fig. 3a shows that the topological hinge state can be well confined at the hinges even if its dispersion is located within the light cone. To excite the topological hinge states, a source antenna (cyan stars in Fig. 3d, e) is placed at the center of the hinge. Subsequently, we use another probe antenna to measure the transmission spectra of the hinge (blue color) and surface (orange color) states, as shown in Fig. 3c, in which the hinge state transmission spectrum exhibits two peaks within the two transmission dips (bandgaps) of the surface states. Figure 3d shows the measured electric field

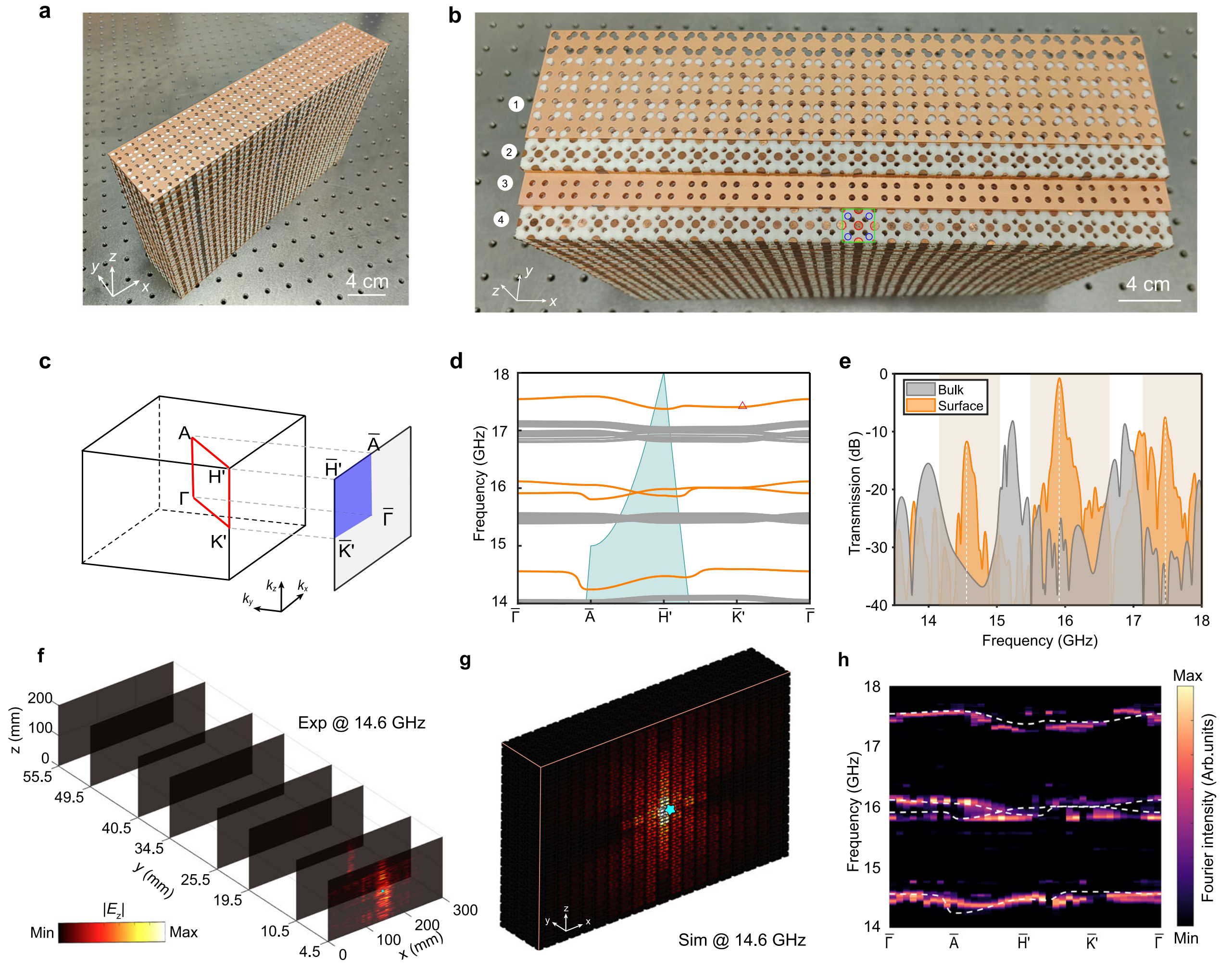

Fig. 2 | Observation of the first-order photonic topological surface states. **a** Photograph of the fabricated experimental sample comprising 4 unit cells in the *y* direction and 20 unit cells in the *x* and *z* directions. **b** The compositional layers are glided for photographing. Each unit cell (green square) comprises two perforated copper plate layers and two air foam layers inserted by metallic pillars (red circles) and dielectric rods (blue circles). **c** Schematic view of the projected 2D surface BZ. **d** Simulated surface (orange lines) and bulk (grey lines) state dispersions along high-symmetry lines. The cyan curve represents the light cone. **e** Measured transmission spectra of the surface (orange color) and bulk (grey color) states. The light beige regions represent the three photonic bandgaps. Measured (**f**) and simulated (**g**) electric field distributions of the topological surface states at 14.6 GHz. The cyan star represents the point source. **h** Measured (color map) and simulated (white dashed line) surface state dispersions along the high symmetry line.

distribution of the topological hinge state at 14.9 GHz, matching well with the simulation result shown in Fig. 3e. The field is predominantly localized on the hinge, indicating the presence of topological hinge states. The measured hinge dispersion (color map) along the k_z direction is obtained through Fourier transformation on the measured hinge states' complex electric field distribution, as shown in Fig. 3f, which shows excellent agreement with the simulation results (white dashed line).

Experimental observation of the third-order photonic topological corner states

We then experimentally characterize the third-order photonic topological corner states in the 3D MCPC. Note that all eight corners of the 3D photonic HOTI can support corner states, and here we only focus on one single corner. We begin by measuring the transmission spectra of the surface (orange color), hinge (blue color), and corner (green color) states under the excitation of a point source (cyan stars in Fig. 4b, c) placed near the corner. As shown in Fig. 4a, the corner measurement exhibits a transmission peak at about 15.8 GHz (white dashed line), which agrees well with the corresponding eigenfrequency ranges of the calculated corner, hinge, and surface eigenstates shown in Fig. 1e. We also plot the measured and simulated electric field distributions of the corner states at 15.8 GHz in Fig. 4b and Fig. 4c, respectively. It can be seen that the electric field distributions are mainly concentrated at the corner, revealing the tightly localized characteristic of the topological corner states.

Experimental demonstration of the robustness of topological surface, hinge, and corner states

Finally, we experimentally demonstrate the robustness of the topological boundary states by introducing defects (removing some dielectric rods) at the surface, hinge, and corner, respectively, as shown in the insets of Fig. 5a–c (red circles) for the experimental measurements and Fig. 5d–f (white dashed cylinder) for the numerical simulations. The measured (Fig. 5a–c) and simulated (Fig. 5d–f) electric field distributions of the topological surface, hinge, and corner states with defects are almost the same as those without defects (Figs. 2–4) except for a sudden decrease in the electric fields at the defect location due to the absence of the dielectric rods, verifying the robustness of the topological surface, hinge, and corner states against defects.

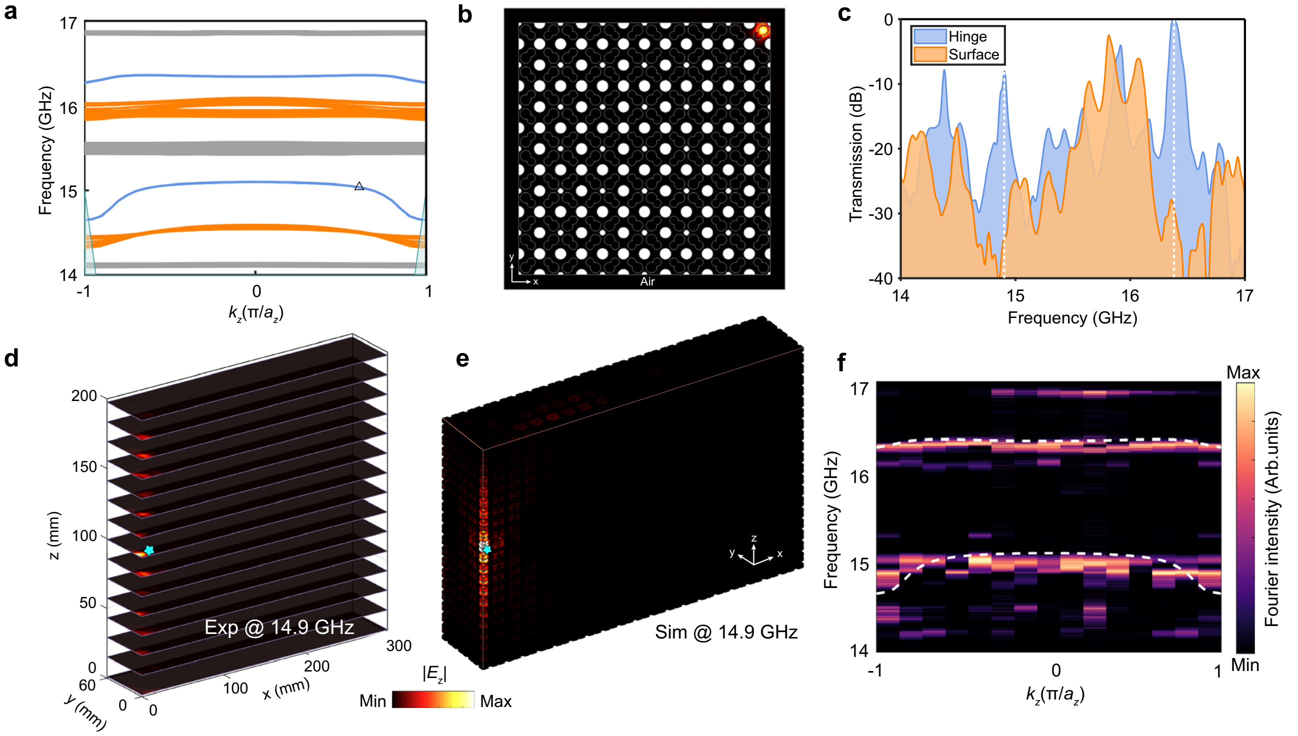

Fig. 3 | Observation of the second-order photonic topological hinge states. **a** Simulated bulk (grey lines), surface (orange lines), and hinge (blue lines) state dispersions along the k_z direction. The cyan curve represents the light cone. **b** Simulated electric field distribution of the hinge states corresponding to the black triangle in **a**. **c** Measured transmission spectra of the hinge (blue color) and surface (orange color) states. Measured (**d**) and simulated (**e**) electric field distributions of the topological hinge states at 14.9 GHz with the source antenna (cyan star) placed at the middle of the hinge. **f** Measured (color map) and simulated (white dashed line) hinge state dispersions along the k_z direction.

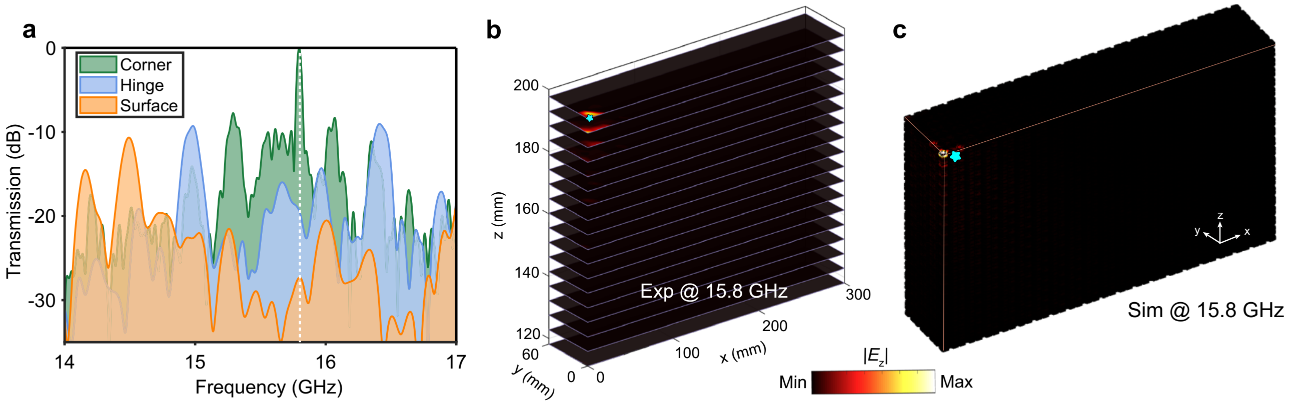

Fig. 4 | Observation of the third-order photonic topological corner states. **a** Measured transmission spectra of the surface (orange color), hinge (blue color), and corner (green color) states. Measured (**b**) and simulated (**c**) electric field distributions of the topological corner states with the source antenna (cyan star) placed near the corner.

Discussion

In conclusion, we have experimentally realized a Wannier-type 3D photonic HOTIs with a dimensional hierarchy of coexisting first-order 2D surface states, second-order 1D hinge states, and third-order 0D corner states in a single 3D MCPC. Moreover, we experimentally demonstrate that all-order photonic topological boundary states are defect-immune and self-guided without any ancillary cladding, making them more suitable for practical applications. The ability to integrate 2D surface states, 1D hinge states, and 0D corner states in a single photonic structure may yield potential applications for multi-dimensional photon steering in 3D photonic devices. Since our work provides a versatile platform for directly mimicking 3D tight-binding models in 3D photonic crystals, we envision more experimental studies on realizing topological lattice defects such as dislocation[57–59] disclination[60] and Dirac vortex[61,62] in 3D photonic crystals. Along these lines, 3D photonic topological insulators and HOTIs operating at telecom or visible frequencies are on the horizon[63,64]. Besides, 3D artificial gauge fields induced by lattice site deformation[65] or 3D non-Hermitian photonics[25] induced by lattice sites' gain and loss are also ready to be explored based on our platform.

Methods

Numerical simulations

All numerical results presented in this work are simulated by the RF module of COMSOL Multiphysics. The bulk band structure is calculated using a unit cell with periodic boundary conditions in all directions. The perforated copper plates and metallic pillars are modeled as perfect electric conductors (PEC). The surface state dispersion is calculated by adopting a $1 \times 4 \times 1$ supercell and applying periodic boundary conditions

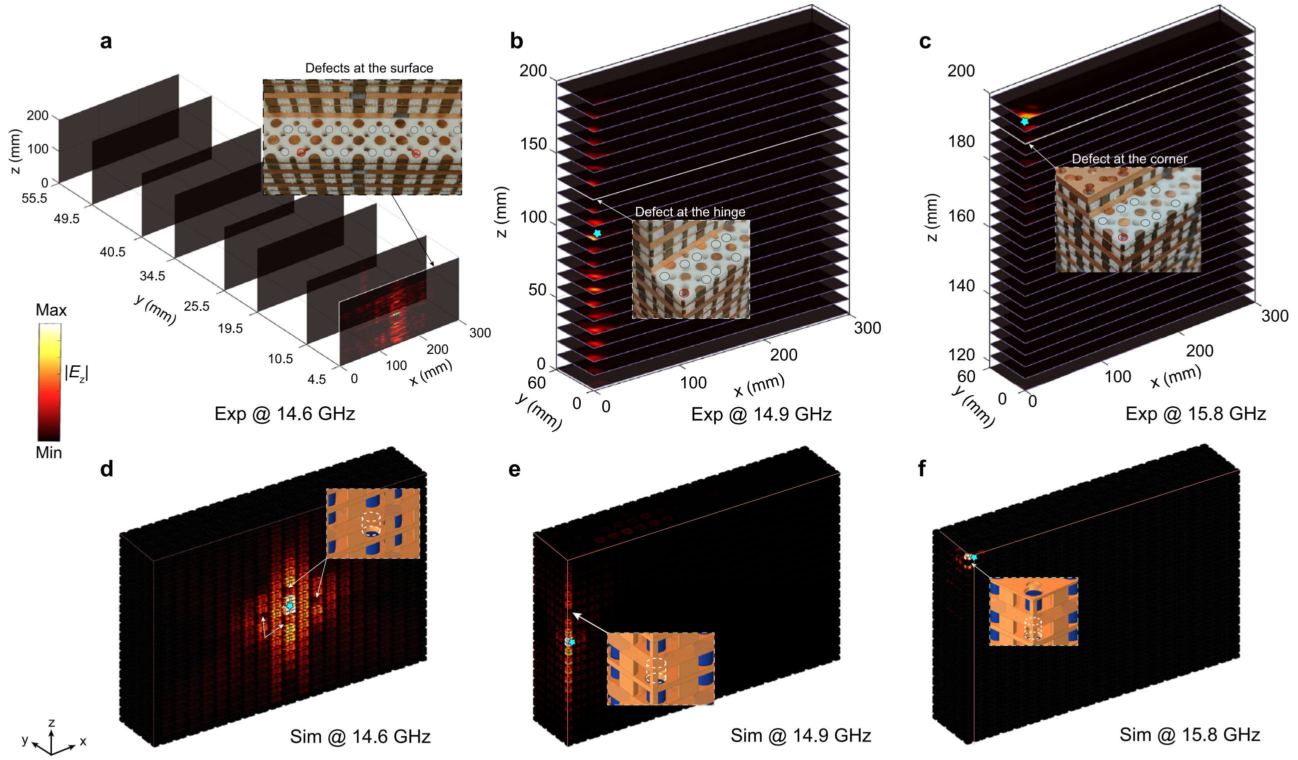

Fig. 5 | Experimental demonstration of the robustness of topological surface, hinge, and corner states. Cutaway views of the measured electric field distributions of the topological surface (**a**), hinge (**b**), and corner (**c**) states with defects, respectively. The insets display photographs of the defects introduced by removing dielectric rods (red circles). Simulated electric field distributions of the topological surface (**d**), hinge (**e**), and corner (**f**) states with defects, respectively. The insets show the defects introduced by removing dielectric rods (white dotted cylinders). The cyan star represents the point source.

along the *x* and *z* directions, and open boundary conditions along the *y* direction. The hinge state dispersion along the *z* direction is calculated using a 6 × 6 × 1 supercell and applying periodic boundary conditions along the *z* direction, and open boundary conditions along the *x* and *y* directions. In the eigenstate and full-wave simulations of a finite 3D photonic crystal, all six boundaries are set as open boundary conditions.

Sample fabrication

The MCPCs are assembled layer by layer and comprise perforated metallic plates, dielectric rods, metal pillars, and perforated air foams. The dielectric rods sintered from alumina have a relative permittivity of 9. The metal pillars are fabricated using surface wire cutting and have a geometric tolerance of about 0.05 mm. The copper plates are fabricated by depositing a 0.035 mm-thick copper layer onto a Teflon woven-glass fabric laminate substrate. We adopt perforated air foam (ROHACELL 31 HF with a relative permittivity of 1.04 and a loss tangent of 0.0025) to fix those metallic pillars and dielectric rods.

Experimental setups

In the experimental measurement, the amplitude and phase of the electric fields are measured by a vector network analyzer (Keysight E5080), connected to two electric dipole antennas with a diameter of 1.2 mm, which serves as the source and probe, respectively. The air holes with a radius of $r_1 = 1.5$ mm (see Fig. 1b and Fig. 2a, b) are carefully designed in MCPCs not only to insert the probe antenna to measure the electric fields in the sample but also to obtain suitable vertical interlayer couplings. The measured transmission spectra of the topological surface, hinge, and corner states in Figs. 2e, 3c, and 4a are obtained using the experimental setup schematically shown in Figure. S14. To measure the transmission spectra of the surface and bulk states in Fig. 2e, a source antenna (cyan star) is positioned at the center of the front surface and a probe antenna is inserted into the surface (orange dot) or bulk (gray dot) through the air hole, located an equal distance away from the source (see Fig. S14a). To measure the transmission spectra of topological hinge and surface states in Fig. 3c, a source antenna (cyan star) is placed at the center of one hinge and a probe antenna is inserted into the same hinge (blue dot) and surface (orange dot) positioned five unit cells away from the source antenna (see Fig. S14b). To measure the transmission spectra of the topological corner, hinge, and surface states in Fig. 4a, a source antenna (cyan star) is positioned near the corner and a probe antenna is placed at the corner (green dot) one unit cell away from the source, hinge (blue dot), and surface (orange dot) five unit cells away from the source (see Fig. S14c).

To measure the electric field distributions of the topological surface, hinge, and corner states, we insert the probe antenna into 320 air holes one by one and scan automatically along the *z*-direction with a 1 mm step length (200 steps). By scanning all the air holes, we can obtain 64000 points of measured data (320 air holes multiply 200 steps) to map the electric field distributions of the topological bulk and boundary states of the 3D photonic HOTIs. Note that since the probe antenna cannot be inserted into the same air hole as the source antenna, the measured data of the air hole with the source antenna has been replaced with measured data from the adjacent air hole. We then perform Fourier transformation to the measured complex electric field distributions at each frequency to obtain the projected band structures of the topological surface and hinge states.

Data availability

All data are available in the manuscript, the supplementary materials, or have been deposited in the Zenodo database. https://doi.org/10.5281/zenodo.14999044

Code availability

We use commercial software COMSOL Multiphysics to perform electromagnetic numerical simulations. Requests for computation details can be addressed to the corresponding authors.

References

1. Kim, M., Jacob, Z. & Rho, J. Recent advances in 2D, 3D and higher-order topological photonics. *Light Sci. Appl* **9**, 130 (2020).
2. Xie, B. Y. et al. Higher-order band topology. *Nat. Rev. Phys.* **3**, 520–532 (2021).
3. Benalcazar, W. A., Bernevig, B. A. & Hughes, T. L. Quantized electric multipole insulators. *Science* **357**, 61 (2017).
4. Langbehn, J., Peng, Y., Trifunovic, L., Oppen, F. & Brouwer, P. W. Reflection-symmetric second-order topological insulators and superconductors. *Phys. Rev. Lett.* **119**, 246401 (2017).
5. Schindler, F. et al. Higher-order topological insulators. *Sci. Adv.* **4**, eaat0346 (2018).
6. Peterson, C. W., Benalcazar, W. A., Hughes, T. L. & Bahl, G. A A quantized microwave quadrupole insulator with topologically protected corner states. *Nature* **555**, 346 (2018).
7. Noh, J. et al. Topological protection of photonic mid-gap defect modes. *Nat. Photon.* **12**, 408 (2018).
8. Mittal, S. et al. Photonic quadrupole topological phases. *Nat. Photon.* **13**, 692 (2019).
9. Chen, X. D. et al. Direct observation of corner states in second-order topological photonic crystal slabs. *Phys. Rev. Lett.* **122**, 233902 (2019).
10. Xie, B. Y. et al. Visualization of higher-order topological insulating phases in two-dimensional dielectric photonic crystals. *Phys. Rev. Lett.* **122**, 233903 (2019).
11. Hassan, A. E. et al. Corner states of light in photonic waveguides. *Nat. Photon.* **13**, 697 (2019).
12. Peterson, C. W., Li, T., Benalcazar, W. A., Hughes, T. L. & Bahl, G. A fractional corner anomaly reveals higher-order topology. *Science* **368**, 1114 (2020).
13. Li, M. et al. Higher-order topological states in photonic kagome crystals with long-range interactions. *Nat. Photon.* **14**, 89–94 (2020).
14. Xie, B. Y. et al. Higher-order quantum spin Hall effect in a photonic crystal. *Nat. Commun.* **11**, 3768 (2020).
15. Cerjan, A., Jürgensen, M., Benalcazar, W. A., Mukherjee, S. & Rechtsman, M. C. Observation of a higher-order topological bound state in the continuum. *Phys. Rev. Lett.* **125**, 213901 (2020).
16. Kim, H. R. et al. Multipolar lasing modes from topological corner states. *Nat. Commun.* **11**, 5758 (2020).
17. Zhang, L. et al. Higher-order topological states in surface-wave photonic crystals. *Adv. Sci.* **7**, 201902724 (2020).
18. Kirsch, M. S. et al. Nonlinear second-order photonic topological insulators. *Nat. Phys.* **17**, 995–1000 (2021).
19. Schulz, J., Noh, J., Benalcazar, W. A., Bahl, G. & Freymann, G. V. Photonic quadrupole topological insulator using orbital-induced synthetic flux. *Nat. Commun.* **13**, 6597 (2022).
20. Wang, Z. et al. Higher-order Dirac semimetal in a photonic crystal. *Phys. Rev. B* **105**, L060101 (2022).
21. Pan, Y. et al. Real higher-order Weyl photonic crystal. *Nat. Commun.* **14**, 6636 (2023).
22. Li, J. et al. Disentangled higher-orbital bands and chiral symmetric topology in confined Mie resonance photonic crystals. *Laser Photon. Rev.* https://doi.org/10.1002/lpor.202300543 (2023).
23. Zhang, Y. X., Dai, X. Y. & Xiang, Y. J. Photonic higher-order topological insulator with enlarged non-trivial bandgaps. *Laser Photon. Rev.* **17**, 202300384 (2023).
24. Zhang, Y. X., Dai, X. Y. & Xiang, Y. J. Dirac hierarchy in confined Mie resonance photonic crystals. *Phys. Rev. B* **109**, 064105 (2024).
25. Wang, X. X. et al. Higher-order states in a non-Hermitian 3D topological photonic crystal. *Laser Photon. Rev.* https://doi.org/10.1002/lpor.202300204 (2023).
26. Yun, J., Kim, S., So, S., Kim, M. & Rho, J. Deep learning for topological photonics. *Adv. Phys.: X* **7**, 2046156 (2022).
27. Xue, H., Yang, Y., Gao, F., Chong, Y. & Zhang, B. Acoustic higher-order topological insulator on a kagome lattice. *Nat. Mater.* **18**, 108 (2019).
28. Ni, X., Weiner, M., Alù, A. & Khanikaev, A. B. Observation of higher-order topological acoustic states protected by generalized chiral symmetry. *Nat. Mater.* **18**, 113 (2019).
29. Zhang, X. et al. Second-order topology and multidimensional topological transitions in sonic crystals. *Nat. Phys.* **15**, 582 (2019).
30. Qi, Y. et al. Acoustic realization of quadrupole topological insulators. *Phys. Rev. Lett.* **124**, 206601 (2020).
31. Xue, H. et al. Realization of an acoustic third-order topological insulator. *Phys. Rev. Lett.* **122**, 244301 (2019).
32. Zhang, X. et al. Dimensional hierarchy of higher-order topology in three-dimensional sonic crystals. *Nat. Commun.* **10**, 5331 (2019).
33. Weiner, M., Ni, X., Li, M., Alù, A. & Khanikaev, A. B. Demonstration of a third-order hierarchy of topological states in a three-dimensional acoustic metamaterial. *Sci. Adv.* **6**, eaay4166 (2020).
34. Ni, X., Li, M., Weiner, M., Alù, A. & Khanikaev, A. B. Demonstration of a quantized acoustic octupole topological insulator. *Nat. Commun.* **11**, 2108 (2020).
35. Xue, H. et al. Observation of an acoustic octupole topological insulator. *Nat. Commun.* **11**, 2442 (2020).
36. He, C. et al. Acoustic analogues of three-dimensional topological insulators. *Nat. Commun.* **11**, 2318 (2020).
37. Zheng, L. Y. & Christensen, J. Dirac hierarchy in acoustic topological insulators. *Phys. Rev. Lett.* **127**, 156401 (2021).
38. Yang, L. et al. Observation of Dirac hierarchy in three-dimensional acoustic topological insulators. *Phys. Rev. Lett.* **129**, 125502 (2022).
39. Wei, Q. et al. 3D hinge transport in acoustic higher-order topological insulators. *Phys. Rev. Lett.* **127**, 255501 (2021).
40. Luo, L. et al. Observation of a phononic higher-order Weyl semimetal. *Nat. Mater.* **20**, 794 (2021).
41. Pu, Z. et al. Acoustic higher-order Weyl semimetal with bound hinge states in the continuum. *Phys. Rev. Lett.* **130**, 116103 (2023).
42. Ma, Q. et al. Observation of higher-order nodal line semimetal in phononic crystals. *Phys. Rev. Lett.* **132**, 066601 (2024).
43. Garcia, M. S. et al. Observation of a phononic quadrupole topological insulator. *Nat. (Lond.)* **555**, 342 (2018).
44. Wu, Y. et al. On-chip higher-order topological micromechanical metamaterials. *Sci. Bull.* **66**, 1959–1966 (2021).
45. Imhof, S. et al. Topolectrical-circuit realization of topological corner modes. *Nat. Phys.* **14**, 925 (2018).
46. Liu, S. et al. Octupole corner state in a three-dimensional topological circuit. *Light.: Sci. Appl.* **9**, 1–9 (2020).
47. Wu, H. et al. Higher-order topological states in thermal diffusion. *Adv. Matter* **35**, 202210825 (2023).
48. Xu, G., Zhou, X., Yang, S., Wu, J. & Qiu, C. W. Observation of bulk quadrupole in topological heat transport. *Nat. Commun.* **14**, 3252 (2023).
49. Kim, M. et al. Extremely Broadband Topological Surface States in a Photonic Topological Metamaterial. *Adv. Opt. Mater.* **7**, 1900900 (2019).
50. Ho, K. M., Chan, C. T. & Soukoulis, C. M. Existence of a photonic gap in periodic dielectric structures. *Phys. Rev. Lett.* **65**, 3152–3155 (1990).
51. Lidorikis, E., Sigalas, M. M., Economou, E. N. & Soukoulis, C. M. Tight-Binding Parametrization for Photonic Band Gap Materials. *Phys. Rev. Lett.* **81**, 1405–1408 (1998).
52. Yang, B. et al. Chan, Scalar topological photonic nested meta-crystals and skyrmion surface states in the light cone continuum. *Nat. Mater.* **22**, 1203 (2023).
53. Yang, Y. et al. Realization of a three-dimensional photonic topological insulator. *Nature* **565**, 622–626 (2019).
54. Liu, G. G. et al. Topological Chern vectors in three-dimensional photonic crystals. *Nature* **609**, 925–930 (2022).

55. Xi, X. et al. Topological antichiral surface states in a magnetic Weyl photonic crystal. *Nat. Commun.* **14**, 1991 (2023).
56. Kim, M. et al. Three-dimensional photonic topological insulator without spin-orbit coupling. *Nat. Commun.* **13**, 3499 (2022).
57. Xue, H. R. et al. Observation of dislocation-induced topological modes in a three-dimensional acoustic topological insulator. *Phys. Rev. Lett.* **127**, 214301 (2021).
58. Ye, L. P. et al. Topological dislocation modes in three-dimensional acoustic topological insulators. *Nat. Commun.* **13**, 508 (2022).
59. Lin, Z. K. et al. Topological Wannier cycles induced by sub-unit-cell artificial gauge flux in a sonic crystal. *Nat. Mater.* **21**, 430–437 (2022).
60. Wang, Q. et al. Vortex states in an acoustic Weyl crystal with a topological lattice defect. *Nat. Commun.* **12**, 3654 (2021).
61. H. B. Cheng, J. Y. Yang, Z. Wang, and L. Lu, Monopole topological resonators, arXiv: 2210.09056 (2023).
62. Ma, J. et al. Observation of vortex-string chiral modes in metamaterials. *Nat. Commun.* **15**, 2332 (2024).
63. Lin, Q., Sun, X., Xiao, M., Zhang, S. & Fan, S. A three-dimensional photonic topological insulator using a two-dimensional ring resonator lattice with a synthetic frequency dimension. *Sci. Adv.* **4**, aat2774 (2018).
64. Lustig, E. et al. Photonic topological insulator induced by a dislocation in three dimensions. *Nature* **609**, 931–935 (2022).
65. Cheng, Z. Y. et al. Three-dimensional flat Landau levels in an inhomogeneous acoustic crystal. *Nat. Commun.* **15**, 2174 (2024).

Acknowledgements

Z.G. acknowledges funding from the National Natural Science Foundation of China under grants No. 62361166627, 62375118, and 12104211, Guangdong Basic and Applied Basic Research Foundation under grant No.2024A1515012770, Shenzhen Science and Technology Innovation Commission under grants No. 20220815111105001 and 202308073000209, High level of special funds under grant No. G03034K004. B.X. acknowledges fundings from the National Key R&D Program of China under grant No. 2023YFA1407700, the National Natural Science Foundation of China under grants No. 62475225 and No. 12404187, GuangDong Basic and Applied Basic Research Foundation under grant No. 2024A1515012031, Shenzhen Science and Technology Innovation Commission under grant No. CYJ20240813113619025, Stable Support Program for Higher Education Institutions of Shenzhen under grant No. 20220817185604001. Y.M. acknowledges the support from the National Natural Science Foundation of China under grant No. 12304484, Basic and Applied Basic Research Foundation of Guangdong Province under grant No. 2414050002552. P.S. acknowledges the National Natural Science Foundation of China under grant No. 62220106006, Shenzhen Science and Technology Program under grant No. SGDX20211123114001001. X.X. acknowledges the support from the National Natural Science-Foundation of China under grant No.62405053, Basic and Applied Basic Research Foundation of Guangdong Province under grant No. 2025A1515012229. Z.X.Z. acknowledges the support from the National Natural Science Foundation of China under Grant No. 12404053, Guangdong Basic and Applied Basic Research Foundation of Guangdong Province under grant No. 2025A1515012284.

Author contributions

Z.G. conceived the idea and initiated the project. Z.Y.W., Y.M., B.Y., and X.X. performed the simulations. Z.Y.W., D.Z., Z.X.Z., B.Y.X, and Z.G designed the experiments. Z.Y.W., D.Z., X.X., M.Q.C., B.Y., L.Y., Y.M., Z.X.Z., J.M.C., and Z.G. fabricated samples. Z.Y.W., D.Z., T.X., and B.Y. carried out the measurements. Z.Y.W., X.X., Z.X.Z., Y.M., B.Y.X, and Z.G. analyzed data. Z.Y.W., Z.G., X.X., and B.Y.X wrote the manuscript with input from G.G.L., Y.H.Y, P.P.S., and H.S.C. Z.G., X.X., Z.X.Z., and B.Y.X. supervised the project.

Competing interests

The authors declare no competing interests.

Additional information

Supplementary information The online version contains supplementary material available at https://doi.org/10.1038/s41467-025-58051-7.

Correspondence and requests for materials should be addressed to Xiang Xi, Zhen-Xiao Zhu, Biye Xie or Zhen Gao.

Peer review information *Nature Communications* thanks Junsuk Rho, and the other, anonymous, reviewer(s) for their contribution to the peer review of this work. A peer review file is available.